Nanoscale

Accepted Manuscript

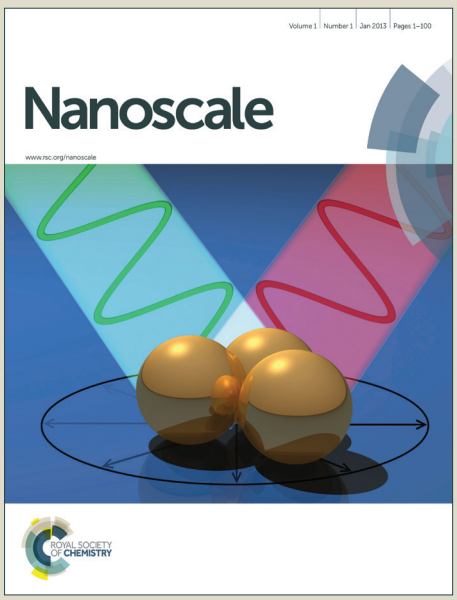

ROYAL SOCIETY OF CHEMISTRY

www.rsc.org/nanoscale

Cite this: DOI: 10.1039/c0xx00000x

www.rsc.org/xxxxxx

ARTICLE TYPE

Antibacterial Activity of Two-Dimensional MoS_2 Sheets

Xi Yang,[a] Jie Li,[b] Tao Liang,[a] Chunyan Ma,[a] Yingying Zhang,[a] Hongzheng Chen,*[a] Nobutaka Hanagata,*[b] Huanxing Su,*[c] and Mingsheng Xu*[a]

Received (in XXX, XXX) Xth XXXXXXXXX 20XX, Accepted Xth XXXXXXXXX 20XX

DOI: 10.1039/b000000x

Graphene-like two-dimensional materials (2DMats) show application potentials in optoelectronics and biomedicine due to their unique properties. However, environmental and biological influences of these 2DMats remain to be uncovered. Here we reported the antibacterial activity of two-dimensional (2D) chemically exfoliated MoS_2 (ce-MoS_2) sheets. We found that the antibacterial activity of ce-MoS_2 sheets was much more potent than that of the raw MoS_2 powders used for the synthesis of ce-MoS_2 sheets possibly due to the 2D planar structure (high specific surface area) and higher conductivity of the ce-MoS_2. We investigated the antibacterial mechanisms of the ce-MoS_2 sheets and proposed their antibacterial pathways. We found that the ce-MoS_2 sheets could produce reactive oxygen species (ROS), different from previous report on graphene-based materials. Particularly, the oxidation capacity of the ce-MoS_2 sheets toward glutathione oxidation showed a time and concentration dependent trend, which is fully consistent with the antibacterial behaviour of the ce-MoS_2 sheets. The results suggest that antimicrobial behaviors were attributable to both membrane and oxidation stress. The antibacterial pathways include MoS_2-bacteria contact induced membrane stress, superoxide anion ($O2^{\bullet-}$) induced ROS production by the ce-MoS_2, and the ensuing superoxide anion-independent oxidation. Our study thus indicates that the tailoring of dimension of nanomaterials and their electronic properties would manipulate antibacterial activity.

Introduction

Graphene is one of the typical two-dimensional layered materials (2DMats) with unique electronic and optical properties and has a wide range of potential applications including for biomedicine.[1] Inspired by the graphene research and development, very recently, graphene-like two-dimensional (2D) materials have gained renewed interest.[2] These 2DMats include transition metal dichalcogenides (TMDs) such as MoS_2,[3] insulating hexagonal boron nitride,[4] silicene,[2,5,6] and other 2D compounds.[2,7] Due to their distinct chemical and crystalline structures, these graphene-like 2DMats exhibit strikingly different properties not only from graphene but also from each other. They have great promise in potential applications[2,7] for nanoelectronics, nanophotonics, hybrid materials, catalysts, energy generation, energy storage, and biomedicine.

MoS_2 is a prototypical TMD material. A single layer MoS_2 consists of two planes of hexagonally arranged sulfur (S) atoms linked to a hexagonal plane of molybdenum (Mo) atoms. In its pristine bulk form the individual layers are held together by weak van der Waals forces. MoS_2 that is a semiconductor displays many intriguing physical and chemical properties with a wide range of potential applications[2] including in dry lubrication,[8] hydrogen evolution,[9] photovoltaics,[10] and sensing.[11] The lacking of inversion symmetry of 2D MoS_2 sheets leads to strong spin-orbit splitting and thus open possibility for spintronic devices.[12,13] The opening of the edges of MoS_2 sheets results in enhanced electrocatalytic hydrogen evolution.[14] 2D MoS_2 sheets also have potentials in biomedical applications. Based on the fluorescence quenching characteristics, Zhu *et al*. showed that MoS_2 monolayers can be used for detection of DNA molecules.[15] By exploiting its near-infrared (NIR) absorbance, MoS_2 sheets have been used as an NIR photothermal agent to kill Hela cells.[16] PEG-functionalized MoS_2 sheets have been reported to have capability for drug delivery.[17] Compared to intensive study of biological effects of graphene, there is absent of a detailed investigation of the possibly toxic effects of 2D MoS_2 materials[16] on the safe use of the materials. Currently, there are only a few studies on the cytotoxicity of 2D MoS_2 sheets in which no obvious toxicity to the Hela cells was found if there was no NIR irradiation,[16] and there is few study on antibacterial behavior of the material.

To realize the potential applications of 2D MoS_2 sheets, we study the antibacterial activity of 2D MoS_2 sheets using a bacterial model, *Escherichia coli* (*E. coli*) with a comparison to the raw MoS_2 powders that were used to synthesize the 2D MoS_2 sheets. We found that 2D MoS_2 sheets showed a more potent antibacterial activity compared with the raw MoS_2 powders. To a better understanding of the antibacterial mechanism, the possibility of superoxide anion induced by reactive oxygen species (ROS) production was evaluated by the 2,3-bis (2-methoxy-4-nitro-5-sulfophenyl)-2*H*-tetrazolium-5-

carboxanilide (XTT) method; and *in vitro* glutathione (γ-L-glutamyl-L-cysteinyl-glycine, GSH) oxidation was used to examine the superoxide anion-independent oxidative stress. Our study suggests that the 2D nature and the electronic properties of the 2D MoS_2 may contribute greatly to their antibacterial activity with membrane and oxidation stress induced by the MoS_2 being proposed underlying mechanisms.

Results and discussion

Antibacterial Activity of MoS_2 Dispersions. We first characterized the physical and chemical properties of the MoS_2 materials used in this study. The MoS_2 materials were the chemically exfoliated MoS_2 (ce-MoS_2) sheets (see Materials and Methods),[18] the raw MoS_2 powders which were used to synthesize the ce-MoS_2 sheets, and the aggregates of ce-MoS_2 sheets (aggregated ce-MoS_2) which were formed after the ce-MoS_2 sheets had been stored in deionized water (DI) for a period time. As observed in Figure 1, these MoS_2 materials show different morphologies. The typical atomic force microscopy (AFM) image (Figure 1a) together with cross-sectional profiles (see Figure S1 in Supporting Information) of the ce-MoS_2 sheets suggests that they are monolayer MoS_2 sheets (with thickness of ~1 nm) and the size of most of the sheets are larger than 200 nm. The raw MoS_2 powders show particle-like features and layered structures, with various sizes up to several micrometers and thickness of 1-2 μm (Figure 1b). The aggregated ce-MoS_2 also shows stacked layer feature (Figure 1c). Contrary to raw MoS_2 powders, the aggregated ce-MoS_2 owns a much thinner thickness (tens of nanometers), which is formed by restacking of monolayer MoS_2 sheets. The Raman spectra of the MoS_2 materials (Figure 2) exhibit different features. Two most intense peaks observed on all the three kinds of MoS_2 materials are related to vibrational modes of E^1_{2g} (around 381.0 cm^{-1}) and A_{1g} (around 409.0 cm^{-1}). The most pronounced peaks of the MoS_2 materials are in agreement with previous studies.[19-21] In the case of the aggregated ce-MoS_2, strong Raman scattering at 1584.5 cm^{-1} were observed, which is quite different from the ce-MoS_2 sheets and the raw MoS_2 powders. Besides these

peaks, we also observed other Raman peaks of the MoS_2 materials, of which further investigations of their origins are needed. Our X-ray photoelectron spectroscopy (XPS) study suggests that the MoS_2 materials are highly pure (see Figure S2 in Supporting Information). A detailed attribution of the most Raman peaks can be found in Supporting Information (Table S1). Furthermore, we performed X-ray diffraction (XRD) measurement to evaluate the crystalline structures of the MoS_2 materials. As shown in Figure S3 (see Supporting Information), compared to the XRD patterns for the raw MoS_2 powder, almost all the peaks disappeared for the ce-MoS_2 sheets and the (002) peak at $2\theta=14.4^o$ became very weak. By contrast, the (002) peak became observable for the aggregated ce-MoS_2, suggesting the monolayer MoS_2 restacking together. The different Raman features and the XRD patterns clearly suggest different crystalline structures of the studied MoS_2 materials.[22-24]

We used *E.coli* DH5α as a model bacterium to evaluate antibacterial activity of ce-MoS_2 sheets. *E.coli* DH5α (10^6 - 10^7 CFU/mL) were incubated with the dispersions of the MoS_2 materials at a concentration ranging from 5 μg/mL - 80 μg/mL in isotonic saline solution at 37 °C under 250 rpm shaking speed for 2 h - 6 h. The isotonic saline solution without MoS_2 materials was used as a control, and control data show that our incubation conditions did not affect the cell viability. The death rate of the bacterial cells was determined by the colony counting method (see Materials and Methods). Figure 3a shows that the ce-MoS_2 sheets exhibited a more toxic effect on the bacteria than the raw MoS_2 powders at all the examined dispersion concentrations. Although the cell viability exposed to the dispersions of raw MoS_2 powders showed little dependence on the dispersion concentration, the dispersion concentrations of ce-MoS_2 sheets had a obvious influence on the bacterial viability (see Figure S4 in Supporting Information). The loss of *E.coli* DH5α viability is 91.8% ± 1.4% after exposed to the ce-MoS_2 dispersion at a concentration of 80 μg/mL, which is more than 2-fold as compared to 38.9% ± 1.2% of the bacteria exposed to 5 μg/mL ce-MoS_2 dispersion. We did not clearly observe

antibacterial activity of the ce-MoS_2 sheets with a concentration less than 1.0 μg/mL for a 2 h exposure, and in the case of the raw MoS_2 powder, the minimum inhibitory concentration were about 2.5 μg/mL.

We also investigated the time dependent antibacterial behavior of the ce-MoS_2 sheets (Figure 3b). *E.coli* DH5α cells were incubated with a dispersion (20 μg/mL) of the ce-MoS_2 sheets for 2 h, 4h, or 6 h. It is found that a large fraction of cell death occurred in the first 2 h incubation. However, Figure 3b shows that the loss of *E.coli* DH5α viability increased from 57.6% ± 2.2% to 93.4% ± 2.7% over incubation time from 2 h to 6 h.

Although ce-MoS_2 sheets can be homogeneously dispersed in DI water, it tends to irreversibly precipitate and aggregate in water within several days. We evaluated the antibacterial effects of aggregated ce-MoS_2 (Figure 3c). We collected the aggregated ce-MoS_2 after the fresh ce-MoS_2 sheets had been dispersed in DI water for 40 days. Just prior to incubating the bacterial cells with the dispersions of MoS_2 materials, we had dispersed the materials by ultrasonication for 10 min. To our surprise, the aggregated ce-MoS_2 even exhibited a lower antibacterial effect than the raw MoS_2 powder. The difference in bacterial viability between the aggregated ce-MoS_2 and the MoS_2 powder might result from the differences in their morphology and crystalline structure. Furthermore, with extending the incubation time, both the aggregated ce-MoS_2 and the raw MoS_2 powder showed a reduced antibacterial effect. This behavior may be due to further aggregation of the ultrasonicated MoS_2 materials even if the incubation was under shaking. These results suggest that the morphology (shape and specific surface area) and crystalline structure have influence on the bacterial viability. It has previously been reported that MoS_2 nanoparticles with size of about 120 nm had no any cytotoxic effect on mammal cells, e.g., A549, K525 and CCC-ESF-1 cell lines up to the nanoparticle concentration of 3.52 μg/mL.[25] The reasons may be attributed to the lower dispersion concentration of

the MoS_2 nanoparticles. It is also noted that different cell lines were used in their study as compared to our present study in which the antibacterial activity of the raw MoS_2 powder was investigated and bacteria are quite different from mammal cells.

Antibacterial Mechanism of MoS_2. Previous studies on the antibacterial behavior of 2D graphene, graphene oxide (GO), and reduced graphene oxide (rGO) have shown that morphology and oxidative stress played important roles in the antibacterial activity.[26-29] Because of the similar 2D planar structure of ce-MoS_2 sheets to these graphene-based materials, we investigated oxidative stress mediated by the ce-MoS_2 sheet and the raw MoS_2 powder in order to explore how ce-MoS_2 sheets kill bacteria.

Normally, oxidative stress may come from different paths. One is dependent on reactive oxygen species (ROS) generated by nanomaterials;[27] another path is ROS-independent oxidative stress, in which nanomaterials may disrupt a specific microbial process through disturbing or oxidizing a vital cellular structure or component without ROS production.[30] We followed the established protocols[29,31] to figure out the possible antibacterial mechanism of the ce-MoS_2 sheets. First, we measured the possibility of superoxide anion ($O_2^{\bullet-}$) production using the XTT method (see Materials and Methods). We used TiO_2 radiated with UV light as a positive control to validate our XTT tests and used XTT along (without MoS_2 materials) as a negative control. As shown in Figure 4, we found different phenomena between the ce-MoS_2 sheet and the raw MoS_2 powder. As compared to the absorbance of XTT along, the ce-MoS_2 sheet enhanced the absorbance at 470 nm, whereas the raw MoS_2 powder suppressed the absorbance. Before the absorption measurement, the mixture of XTT in phosphate buffered saline (PBS) and the MoS_2 materials was filtered through a 0.20 μm surfactant-free cellulose acetate membrane filter. Note that most of our ce-MoS_2 sheets are larger than 200 nm (Figure 1 and Supporting Information) and the absorption peak of exfoliated MoS_2 monolayers localizes at the

wavelength above 600 nm,[32] thus we rule out the interference induced by MoS_2 materials. The results indicate that in contrast to the raw MoS_2 powder, the ce-MoS_2 sheet produced at least some kind of superoxide anion. Our observation is different from the graphene-based materials reported by Liu *et al*.[29] where no noticeable absorption associated with the production of superoxide anion by graphene-based materials was detected. Our XTT test results suggest that ROS can be produced by the ce-MoS_2 sheet but not by the raw MoS_2 powder, and this may contribute to the observed different antibacterial activities between the ce-MoS_2 sheet and the raw MoS_2 powder.

We further used *in vitro* GSH oxidation to examine the possibility of ROS-independent oxidative stress because this path has been reported to play a major role in the antibacterial activity of graphene-based materials.[29] GSH is a tripeptide with thiol groups. The thiol groups (-SH) can be oxidized to disulfide (-S-S-), converting GSH to glutathione disulfide. GSH is an antioxidant in bacteria at a concentration in the range from 0.1 to 10.0 mM[33] preventing damages to cellular components caused by oxidative stress.[34] GSH has been widely used as an oxidative stress indicator in cells.[29,31,35,36] We employed the Ellman's assay[37] to evaluate the oxidation of GSH when it was incubated with ce-MoS_2 sheet and raw MoS_2 powder (see Materials and Methods). Bicarbonate buffer (50.0 mM at pH8.6) and H_2O_2 (1.0 mM) without MoS_2 materials were used as a negative control and a positive control in GSH oxidation experiments, respectively. The negative control suggests that our incubation conditions could not cause GSH oxidation. As shown in Figure 5, the ce-MoS_2 sheet had higher oxidation capacity toward GSH than the raw MoS_2 powder. The oxidation capacity of the raw MoS_2 powder toward GSH was less than 20% and showed little dependence on the concentration in the range from 20 μg/mL to 80 μg/mL during the incubation period up to 6 h. By contrast, the oxidation capacity of ce-MoS_2 sheet toward GSH showed dependence on its concentration and incubation time. In the concentration ranging from 40 μg/mL to 80 μg/mL, the ce-MoS_2 sheet exhibited almost the same

oxidation capacity. In the case of 2 h incubation, the oxidation capacity (68.7% ± 1.9%) of 40 μg/mL dispersion of ce-MoS_2 sheets was more than 2-fold as compared to that (29.5% ± 2.0%) of 20 μg/mL dispersion of ce-MoS_2 sheets (Figure 5a). However, with increase in incubation time, the capacity difference became narrow (Figure 5b). The oxidation capacity of the ce-MoS_2 sheet and raw MoS_2 powder toward GSH is clearly illustrated by the colour change (see Figure S5 in Supporting Information). This incubation time and concentration dependent oxidation capacity is well consistent with the antibacterial activity as observed in Figure 3.

Previously, we have reported that electronic property of SiO_2, CeO_2, ZnO, Al_2O_3, and CuO nanoparticles played an important role in the cytotoxicity of NIH3T3 and A549 cell lines.[38,39] It has also shown that the extent of GSH oxidation was increased with increase in conduction of graphene-based materials[29] and carbon nanotubes.[31] In general, ce-MoS_2 sheets consist of a mixture of two distinct phases, i.e., prismatic 2H and octahedral 1T phases, compared to 2H phase naturally in MoS_2 powders,[40] which is confirmed by our XPS measurement (Figure 6). We found that the our ce-MoS_2 sheets and the aggregated ce-MoS_2 are predominantly in 1T phase, reaching 80.2% and 73.8% calculated from the XPS measurements, respectively, whereas the raw MoS_2 powders are nearly 100% 2H phase. It has been reported that incurred by the phase transition from 2H to 1T phase, there is a dramatic change in the density of states which renders 1T-MoS_2 metallic.[41] This indicates that the conductivity of the ce-MoS_2 sheet and aggregated ce-MoS_2 could be higher than the raw MoS_2 powder (2H phase). Higher conductivity could render lower resistance for electron transfer from bacterial intracellular components to the external environment.[31,38] On the other hand, although the aggregated ce-MoS_2 contained comparable phase compositions (1T phase of 73.8%) with the ce-MoS_2 sheets (1T phase of 80.2%), they exhibited quite different antibacterial activity from the ce-MoS_2 sheets. This may be due to difference of dispersibility, surface area, and size of the MoS_2 materials as discussed

below. Similar phenomena have been previously observed on rGO and GO.[29] For instance, due to stable dispersion and small size of the GO than the easily aggregated rGO, insulating GO exhibited more stronger antibacterial activity than conducting rGO, though rGO had higher oxidation capacity of GSH. The strong oxidation of GSH by the ce-MoS_2 sheets supports that the sheets are capable of oxidizing thiols or other cellular components and consequently make bacteria dead. Despite possible production of ROS by the ce-MoS_2 sheet, the time and concentration dependent incremental trend observed in the antibacterial activity of the ce-MoS_2 sheets suggests that ROS-independent oxidative stress path may dominate the antibacterial activity of the MoS_2 materials.

The similar antibacterial behaviors between the aggregated ce-MoS_2 and the raw MoS_2 powder may suggest that morphology and size are important factors to influence cell-material contact and regulate charge transfer process between the MoS_2 materials and cells. The reduced antibacterial activity with incubating time of the aggregated ce-MoS_2 and raw MoS_2 powders may indicate that both the materials could easily precipitate during the incubation even under shaking. The precipitation would decrease contact area with bacteria. The stable dispersion of 2D ce-MoS_2 sheets during the incubation could translate that they have much larger specific surface area than the raw MoS_2 powder and the aggregated ce-MoS_2 and offer more opportunities to interact with the cells. It has been reported that the edge of ce-MoS_2 sheets is active sites for electrocatalytic hydrogen evolution.[14] The larger surface area together with open edges could make the ce-MoS_2 sheets effectively interact more bacteria and thus offer more efficient pathways for electron transfer reaction between the ce-MoS_2 sheets and the bacteria. In the case of the aggregated ce-MoS_2, even if they have comparable phase compositions (1T and 2H phases) with the ce-MoS_2 sheets, the possible electron transfer between the aggregated ce-MoS_2 and the cells could be greatly reduced because such electron transfer passageways were cut off due to absence of efficient contact. Therefore, the key physicochemical factors govern the antibacterial

activity of the ce-MoS_2 sheets may be the planar nature of the sheets and its induced large specific surface area and electronic properties of the materials.

A three-step antibacterial mechanism has previously been proposed for carbon-based nanomaterials,[29,31] including direct bacterium-nanomaterial contact, intimate membrane disruptive interaction, and then disrupting a specific microbial process by disturbing or oxidizing a vital cellular structure or component. We reason that this basically antibacterial mechanism is also applicable to the MoS_2 materials. The *E.coli* DH5α may first directly contact with the MoS_2 materials, which could be strongly influenced by the surface area of MoS_2 materials. Once contacted, sharp edges of the ce-MoS_2 sheets might cause significant membrane stress like "cutters", disrupting and damaging cell membrane (see Figure S6 in Supporting Information) and in turn leading to the release of intracellular contents and eventually cell death. The production of superoxide anion and in particular the strong oxidation of GSH by the ce-MoS_2 sheets suggest that the sheets could oxidize bacterial components such as lipids, proteins, and DNA.

Conclusions

The antibacterial activity of 2D ce-MoS_2 sheets was evaluated by colony counting method. Incubation *E.coli* DH5 with 80 μg/mL dispersion of ce-MoS_2 sheets for 2 h caused more than 90% of the bacteria death, whereas the dispersion of raw MoS_2 powders which were used to synthesize the ce-MoS_2 killed less than 40% of the cells. The potent antibacterial capacity of the ce-MoS_2 sheet is mostly due to the large specific surface area of the 2D ce-MoS_2 sheet and its higher conductivity originating from the metallic 1T phase compared to the raw MoS_2 powder and the aggregated ce-MoS_2. The antibacterial activity of MoS_2 materials may be attributed to both membrane and oxidative stress. The 2D plane of the ce-MoS_2 sheets could provide more effective contact area with the bacteria, which subsequently induces membrane stress. Interestingly, the XTT test showed that the ce-MoS_2 sheets could produce

ROS. This is different from graphene-based materials that could not produce ROS. The oxidation capacity of the ce-MoS_2 sheet toward GSH showed a time and concentration dependent trend, which is consistent with the antibacterial behavior of the ce-MoS_2 sheets. This suggests that the ce-MoS_2 sheets are capable of inducing superoxide anion-independent oxidative stress. Our study demonstrates that antibacterial activity can be manipulated by tailoring the dimension of nanomaterials such as TMDs and their electronic properties.

Experimental Section

Preparation of ce-MoS_2 and physicochemical characterization: Chemically exfoliated MoS_2 (ce-MoS_2) sheets were synthesized through Li intercalation. 0.3 g raw MoS_2 powders (Sigma-Aldrich) were immersed in 3 mL of 1.6 M butyllithium solution in hexane for 2 days in glovebox. The $LixMoS_2$ was filtrated and washed with hexane to remove excess lithium and organic residues. Exfoliation was achieved immediately by ultrasonicating $LixMoS_2$ in water (10 mg/mL) for 2 h. Exfoliated MoS_2 solution was then dialyzed using MW 10,000 cut-off membranes for 5 days, followed by 4000 rpm centrifugation to remove any un-exfoliated powders. Atomic force microscopy (AFM) images were taken by a Veeco Multimode AFM operated in the tapping mode. Scanning electron microscope (SEM) images were acquired by scanning electron microscopy (SEM, HITACHI S4800, 5 kV, 10 μA). The Raman measurements with the excitation laser line 532 nm were performed using Renishaw inVia Raman microscope system in air ambient environment. The powers of the excitation laser lines were kept well below 1 mW to avoid heating effect. XPS measurement was conducted using an integrated ultrahigh vacuum system equipped with multi-technique surface analysis system (Thermo ESCALAB 250Xi).

Cell Preparation: *E. coli* DH5α was grown in Luria Bertani (LB) medium at 37 ºC, and harvested in the mid-exponential growth phase. The cell culture was centrifuged at 6000 rpm for 10 min to collect

cells, and cells were washed three times with isotonic saline solution to remove residual macromolecules and other growth medium constituents. Bacterial cell suspension was diluted in isotonic saline solution to obtain cell samples containing 10^6 to 10^7 CFU/mL for antibacterial evaluation.

Cell Viability Assessment: The MoS_2 materials were dispersed in deionized (DI) water with difference concentrations for use. *E. coli* DH5α cells were incubated with dispersions comprising of ce-MoS_2 sheet, raw MoS_2 powder, or aggregated ce-MoS_2 in isotonic saline solutions at 37 °C under 250 rpm shaking speed for time up to 6 h. Isotonic saline solution without MoS_2 materials was used as control. The loss of viability of *E. coli* cells was evaluated by colony counting method. Briefly, series of 10-fold cell dilutions (100 μL each) were spread onto LB plates, and left to grow overnight at 37 °C. Colonies were counted and compared with those on control plates to calculate changes in the cell growth inhibition. All tests were prepared in duplicate, and repeated at least on two separate occasions.

Detection of Superoxide Radical Anion ($O_2^{\bullet-}$): To find out the reactive oxygen species antibacterial paths, the possibility of superoxide radical anion ($O_2^{\bullet-}$) production was evaluated by measuring the absorption of XTT (2,3-bis (2-methoxy-4-nitro-5-sulfophenyl)-2*H*-tetrazolium-5-carboxanilide, Fluka). XTT can be reduced by superoxide radical anion ($O^{2\bullet-}$) to form water-soluble XTT-formazan that has maximum absorption at 470 nm. Detail protocol is described in Supporting Information.

Thiol Oxidation and Quantification: Following the method used in a previous study,[29,31] the concentration of thiols in GSH was quantified by the Ellman's assay.[37] The dispersion of ce-MoS_2 sheet or raw MoS_2 powder (225 μL at 20 μg/mL, 40 μg/mL, or 80 μg/mL) in 50 mM bicarbonate buffer (pH 8.6) was added into 225 μL of GSH (0.8 mM in the bicarbonate buffer) to initiate oxidation.

The mixtures were covered with alumina foil to prevent illumination, and then placed in a shaker with a speed of 150 rpm at room temperature for incubation of 2 h - 6 h. After incubation, 785 μL of 0.05 M Tris-HCl and 15 μL of DNTB (Ellman's reagent, 5,5′-dithio-bis-(2-nitrobenzoic acid), Sigma-Aldrich) were added into the mixtures to yield a yellow product. The ce-MoS_2 sheets or raw MoS_2 powders were removed from the mixtures by filtration through a 0.20 μm surfactant-free cellulose acetate membrane filter (Thermo Scientific Nalgene Syringe Filter). A 250 μL aliquot of filtered solutions from each sample was then placed in a 96-well plate. All tests were prepared in triplicate. Their absorbance at 412 nm was measured on a microplate spectrophotometer (MTP-880, Corona Electric Co. Ltd, Japan). GSH solution without MoS_2 materials was used as a negative control. GSH (0.4 mM) oxidization by H_2O_2 (1 mM) was used as a positive control. The measurement was repeated at least on three separate occasions. The loss of GSH was calculated by the following formula: loss of GSH % = (absorbance of negative control – absorbance of sample)/absorbance of negative control × 100.

Notes and references

[a] State Key Laboratory of Silicon Materials, MOE Key Laboratory of Macromolecular Synthesis and Functionalization, Department of Polymer Science and Engineering, Zhejiang University, Hangzhou 310027, P. R. China
E-mail: msxu@zju.edu.cn, hzchen@zju.edu.cn

[b] Interdisciplinary Laboratory for Nanoscale Science and Technology, National Institute for Materials Science, 1-2-1 Sengen, Tsukuba, Ibaraki 305-0047, Japan
E-mail: Hanagata.nobutaka@nims.go.jp

[c] State Key Laboratory of Quality Research in Chinese Medicine and Institute of Chinese Medical Sciences, University of Macau, Macau SAR, P. R. China
E-mail: huanxingsu@umac.mo

†Electronic Supplementary Information (ESI) available: [Superoxide radical anion production experiments and GSH oxidation experiments by MoS_2 materials; Raman peaks of the MoS_2 materials; AFM cross-sectional profile analyses of the ce-MoS_2 sheets; XPS survey spectra of the MoS_2 materials; XRD patterns of the MoS_2 materials; digital camera photos of live *E.coli* DH5α bacteria after they were exposed to ce-MoS_2 dispersions with different concentrations for 2 h; glutathione oxidation by monitoring color change; Keynece Microscope images of the cells exposed to ce-MoS_2 sheets and raw MoS_2 powders.]. See DOI: 10.1039/b000000x/

Acknowledgements

This work was supported by Zhejiang Provincial Natural Science Foundation of China (Youth Talent Program: R4110030), Science and Technology Department of Zhejiang Province (Qianjiang Talent Program:2011R10077), the Program for New Century Excellent Talents in University (NCET-12-0494), the Research Fund for the Doctoral Program of Higher Education (20130101110123), the Program for 14th China-Japan S&T Cooperation (2013DFG52800), and by the Interdisciplinary Laboratory for Nanoscale Science and Technology of National Institute for Materials Science (NIMS), Japan

1 D. Bitounis, H. Ali-Boucetta, B. H. Hong, D. Min and K. Kostarelos, *Adv. Mater*., 2013, ***25***, 2258.

2 M. S. Xu, T. Liang, M. M. Shi and H. Z. Chen, *Chem. Rev*., 2013, ***113***, 3766.

3 K. F. Mak, C. Lee, J. Hone, J. Shan and T. F. Heinz, *Phys. Rev. Lett*., 2010, ***105***, 136805.

4 M. S. Xu, D. Fujita, H. Z. Chen and N. Hanagata, *Nanoscale*, 2011, ***3***, 2854.

5 A. Kara, H. Enriquez, A. P. Seitsonen, L. C. L. Y. Voon, S. Vizzini,; B. Aufray and H. Oughaddou, *Surf. Sci. Rep*., 2012, ***67***, 1.

6 R. Wang, X. D. Pi, Z. Y. Ni, Y. Liu, S. S. Lin, M. S. Xu and D. R. Yang, *Sci. Rep*., 2013, ***3***, 3507.

7 A. K. Geim and I. V. Grigorieva, *Nature*, 2013, ***499***, 419.

8 C. Lee, Q. Y. Li, W. Kalb, X. Z. Liu, H. Berger, R. W. Carpick and J. Hone, *Science*, 2010, ***328***, 76.

9 A. B. Laursen, S. Kegnæs, S. Dahla and I. Chorkendorffa, *Energy Environ. Sci*., 2012, ***5***, 5577.

10 J. Puthussery, S. Seefeld, N. Berry, M. Gibbs and M. Law, *J. Am. Chem. Soc*., 2011, ***133***, 716.

11 H. Li, Z. Y. Yin, Q. Y. He, H. Li, X. Huang, G. Lu, D. W. H. Fam, A. I. Y. Tok, Q. Zhang and H. Zhang, *Small*, 2012, ***8***, 63.

12 H. L. Zeng, J. F. Dai,; W. Yao, D. Xiao and X. D. Cui, *Nature Nanotechnol*., 2012, ***7***, 490.

13 T. Cao, G. Wang, W. P. Han, H. Q. Ye, C. R. Zhu, J. R. Shi, Q. Niu, P. H. Tan, E. G. Wang, B. L. Liu and J. Feng, *Nature Commun*., 2012, ***3***, 887.

14 J. Kibsgaard, Z. Chen, B. N. Reinecke and T. F. Jaramillo, *Nature Mater*., 2012, ***11***, 963.

15 C. Zhu, Z. Zeng, H. Li, F. Li, C. Fan and H. Zhang, *J. Am. Chem. Soc*., 2013, ***135***, 5998.

16 S. S. Chou, B. Kaehr, J. Kim, B. M. Foley, M. De, P. E. Hopkins, J. X. Huang, C. J. Brinker and V. P. Dravid. *Angew. Chem. Int. Ed*., 2013, ***52***, 4160.

17 T. Liu, C. Wang, X. Gu, H. Gong, L. Cheng, X. Z. Shi, L. Z. Feng, B. Q. Sun and Z. Liu, *Adv. Mater*., 2014, ***26***, 3433.

18 X. Yang, W. F. Fu, W. Q. Liu, J. H. Hong, Y. Cai, C. H. Jin, M. S. Xu, H. B. Wang, D. R. Yang and H. Z. Chen, *J. Mater. Chem. A*, 2014, ***2***, 7727.

19 H. Li, Q. Zhang, C. C. R. Yap, B. K. Tay, T. H. T. Edwin, A. Olivier and D. Baillargeat, *Adv. Funct. Mater*., 2012, ***22***, 1385.

20 Y. Wang, C. Cong, C. Qiu and T. Yu, *Small*, 2013, ***9***, 2857.

21 K. Gołasa,; M. Grzeszczyk, P. Leszczynski, C. Faugeras, A. A. L. Nicolet, A. Wysmołek, M. Potemski and A. Babinski, *Appl. Phys. Lett*., 2014, ***104***, 092106.

22 M. Viršek, A. Jesih, I. Miloševic´, M. Damnjanovic´ and M. Remškar, *Surf. Sci*., 2007, ***601***, 2868.

23 R. R. Sahoo and S. K. Biswas, *Tribol. Lett*., 2010, ***37***, 313.

24 B. C. Windom, W. G. Sawyer and D. W. Hahn, *Tribol. Lett*., 2011, ***42***, 301.

25 H. H. Wu, R. Yang, B. M. Song, Q. S. Han, J. Y. Li, Y. Zhang, Y. Fang, R. Tenne and C. Wang, *ACS Nano*, 2011, ***5***, 1276.

26 W. Hu, C. Peng, W. Luo, M. Lv, X. Li, D. Li, Q. Huang and C. Fan, *ACS Nano*, 2010, ***4***, 4317.

27 Y. B. Zhang, S. F. Ali, E. Dervishi, Y. Xu, Z. R. Li, D. Casciano and A. S. Biris, *ACS Nano*., 2010, ***4***, 3181.

28 O. Akhavan and E. Ghaderi, *ACS Nano*, 2010, ***4***, 5731.

29 S. Liu, T. H. Zeng, M. Hofmann, E. Burcombe, J. Wei, R. R. Jiang, J. Kong and Y. Chen, *ACS Nano*, 2011, ***5***, 6971.

30 D. Y. Lyon, L. Brunet, G. W. Hinkal, M. R. Wiesner and P. J. J. Alvarez, *Nano Lett*., 2008, ***8***, 1539.

31 C. D. Vecitis, K. R. Zodrow, S. Kang and M. Elimelech, *ACS Nano*, 2010, ***4***, 5471.

32 G. Eda and S. A. Maier, *ACS Nano*, 2013, ***7***, 5660.

33 R. C. Fahey, W. C. Brown, W. B. Adams and M. B. Worsham, *J. Bacteriol*., 1978, ***133***, 1126.

34 A. Pompella, A. Visvikis, A. Paolicchi, V. D. Tata and A. F. Casini, *Biochem. Pharmacol*., 2003, ***66***, 1499.

35 D. Y. Lyon and P. J. J. Alvarez, *Environ. Sci. Technol*., 2008, ***42***, 8127.

36 O. Carmel-Harel and G. Storz, *Annu. Rev. Microbiol*., 2000, ***54***, 439.

37 G. L. Ellman, *Arch. Biochem. Biophys*., 1959, ***82***, 70.

38 M. S. Xu, D. Fujita, S. Kajiwara, T. Minowa, X. L Li, T. Takemura, H. Iwai and N. Hanagata, *Biomaterials*, 2010, ***31***, 8022.

39 M. S. Xu, J. Li, N. Hanagata, H. X. Su, H. Z. Chen and D. Fujita, *Nanoscale*, 2013, ***5***, 4763.

40 G. Eda, H. Yamaguchi, D. Voiry, T. Fujita, M. W. Chen and M. Chhowalla, *Nano Lett*., 2011, ***11***, 5111.

41 L.f. Mattheis, *Phys. Rev. B*, 1973, ***8***, 3719.

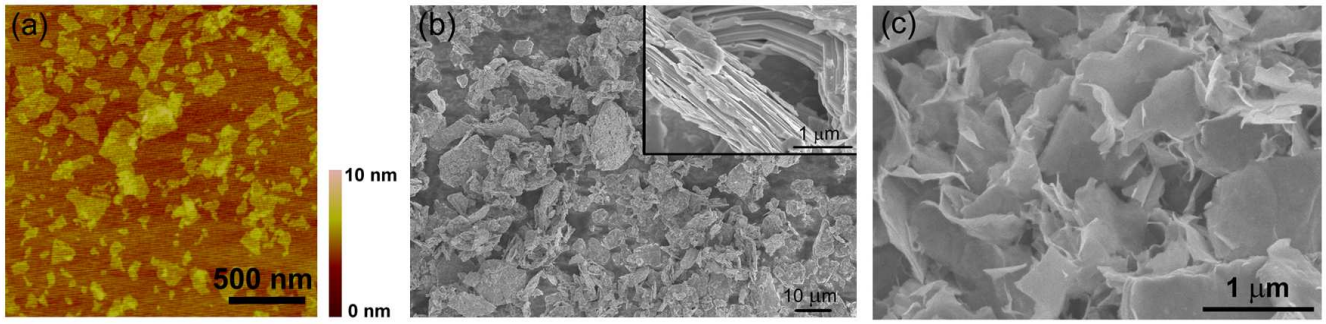

Figure 1. **Morphological characteristics of MoS_2 materials**. (a) Typical AFM image of ce-MoS_2 sheets, (b) Typical SEM image of raw MoS_2 powders (the inset shows the cross section of the layered structure), (c) Typical SEM image of aggregated ce-MoS_2.

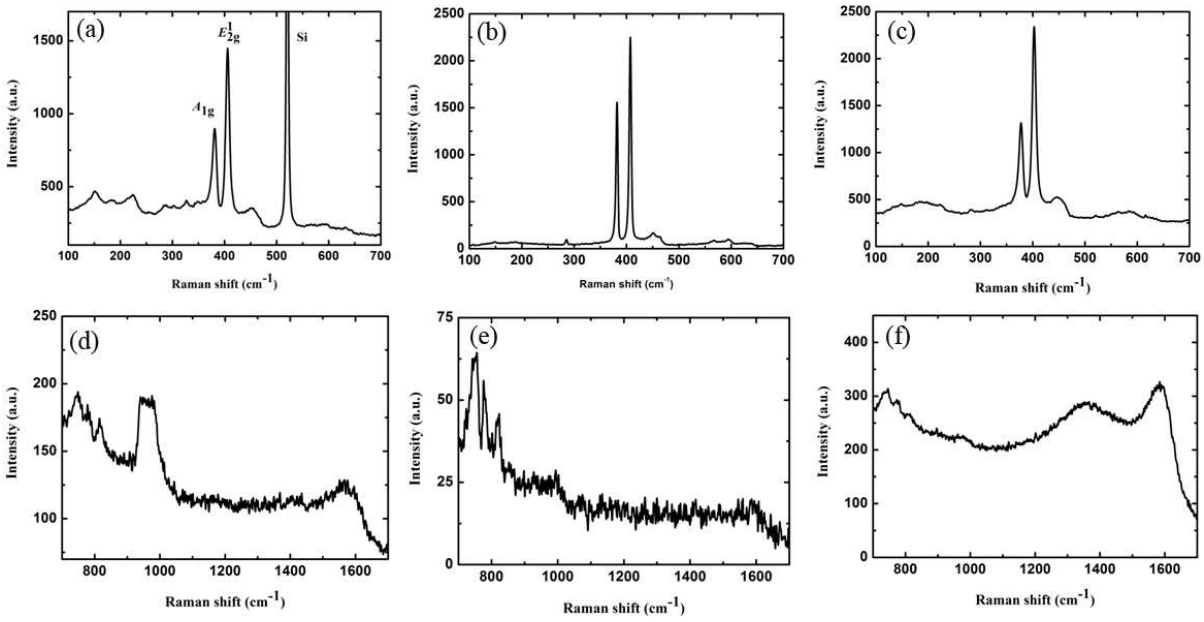

Figure 2. Typical Raman spectra of MoS_2 materials on Si/SiO_2 substrate. (a) and (d) monolayer ce-MoS_2, (b) and (e) Raw MoS_2 powder, (c) and (f) Aggregated ce-MoS_2. The attribution of most of the pronounced peaks can be found in Supporting Information.

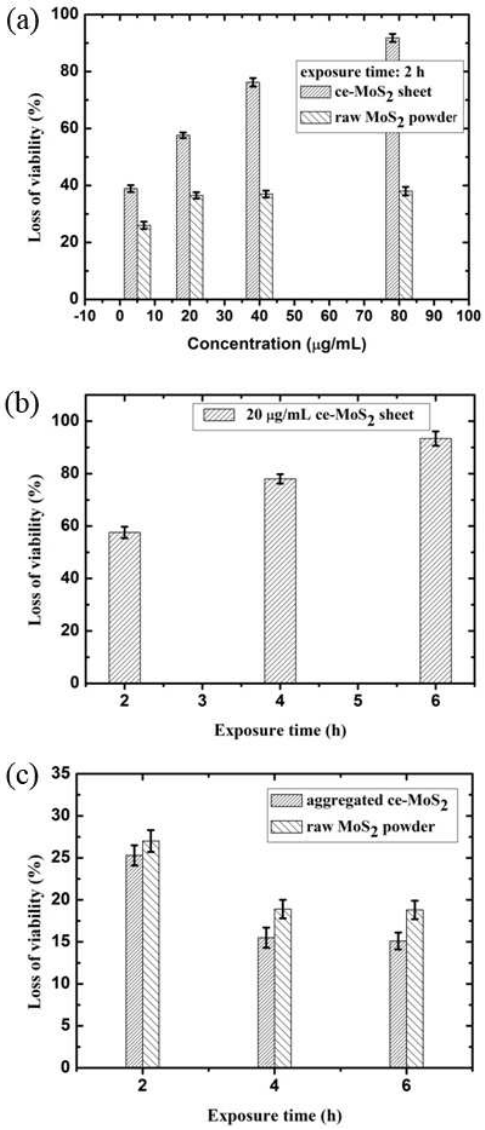

Figure 3. ***E.coli*** **DH5α viability after incubated with dispersions of MoS_2 materials.** (a) Concentration dependent loss of viability of the cells incubated with dispersions of ce-MoS_2 sheets or raw MoS_2 powders at different concentrations for 2 h. (b) Time dependent loss of viability of the cells incubated with a dispersion (20 μg/mL) of ce-MoS_2 sheets for different exposure times. (c) Antibacterial activity of a dispersion (20 μg/mL) of the aggregated ce-MoS_2 as compared to a dispersion (20 μg/mL) of the raw MoS_2 powders for different incubation times. Error bars represents the standard deviation. Isotonic saline solution without MoS_2 materials was used as a control.

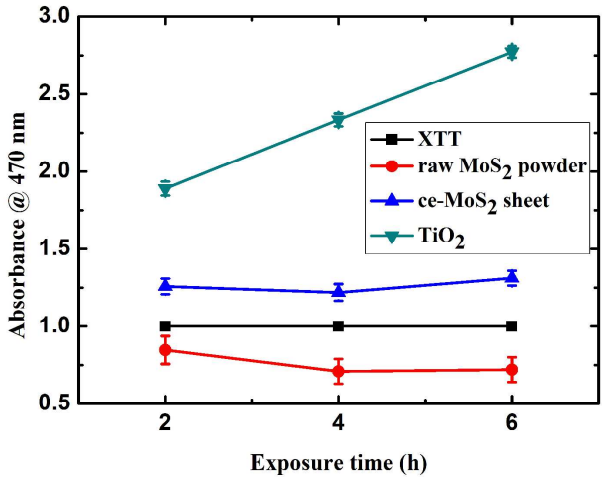

Figure 4. **Production of superoxide radical anion ($O^{2\bullet-}$) by ce-MoS_2 sheets and raw MoS_2 powders.** The dispersion concentrations of the ce-MoS_2 and the raw MoS_2 was 80 μg/mL. The $O^{2\bullet-}$ production was monitored during the incubation of XTT with the MoS_2 materials at pH7.0 in dark. Incubation with TiO_2 under UV radiation was performed as a positive control. XTT along was used as a negative control. The data were plotted by normalized the absorbance of XTT along.

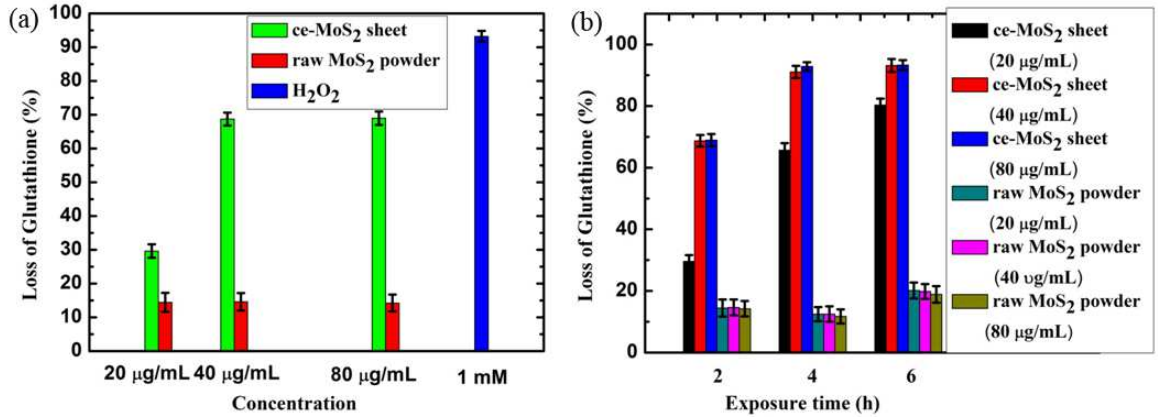

Figure 5. **Oxidation of glutathione by ce-MoS_2 sheets and raw MoS_2 powders.** (a) Loss of GSH (0.4 mM) after *in vitro* incubation with ce-MoS_2 or raw MoS_2 dispersions with different concentrations for 2 h. H_2O_2 (1 mM) was used as a positive control. The bicarbonate buffer without MoS_2 materials was used as a negative control (see Supporting Information.). (b) Time and concentration dependent GSH oxidation of ce-MoS_2 and raw MoS_2 dispersions. The color change induced by the oxidation can be found in Supporting Information.

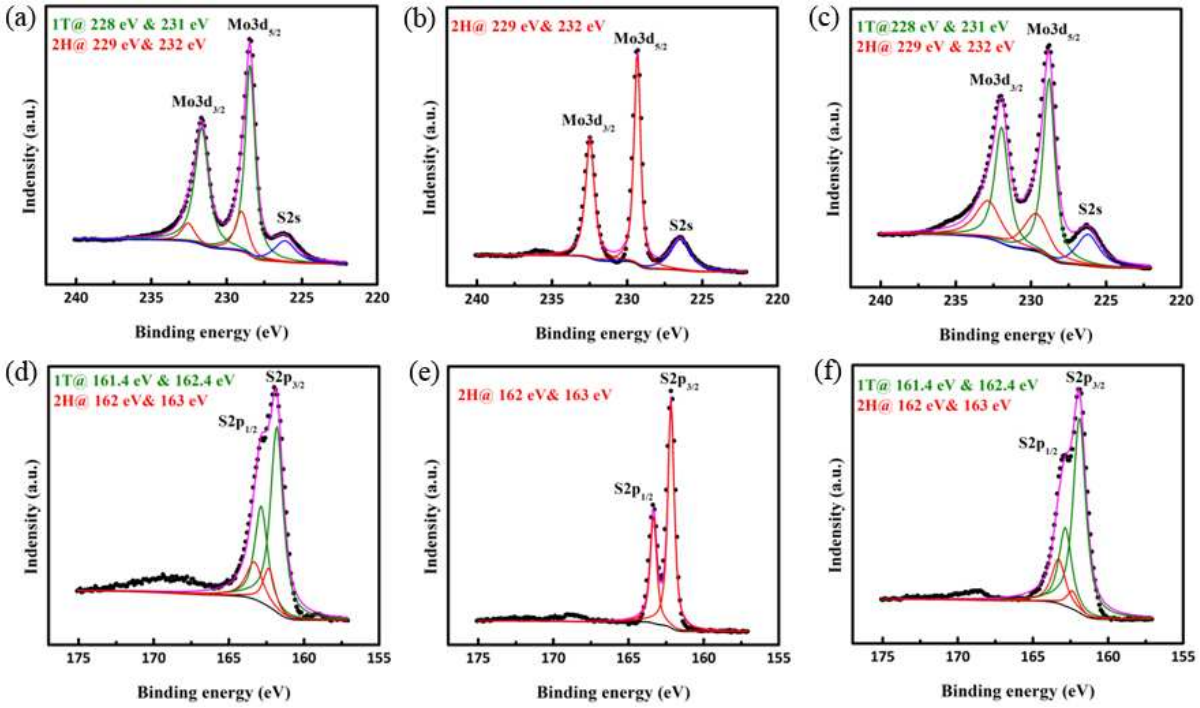

Figure 6. **XPS spectra of Mo3d, S2s, and S2p core level peaks of MoS_2 materials.** (a) Mo3d and S2s patterns of ce-MoS_2 sheet, (b) Mo3d and S2s patterns of raw MoS_2 powder, (c) Mo3d and S2s patterns of aggregated ce-MoS_2, (d) S2p pattern of ce-MoS_2 sheets, (e) S2p pattern of raw MoS_2 powder, (f) S2p pattern of aggregated ce-MoS_2. After Shirley background subtraction, the Mo3d and S2p peaks were de-convoluted to show the 2H and 1T phase contributions, represented by green and red plots, respectively.

TOC

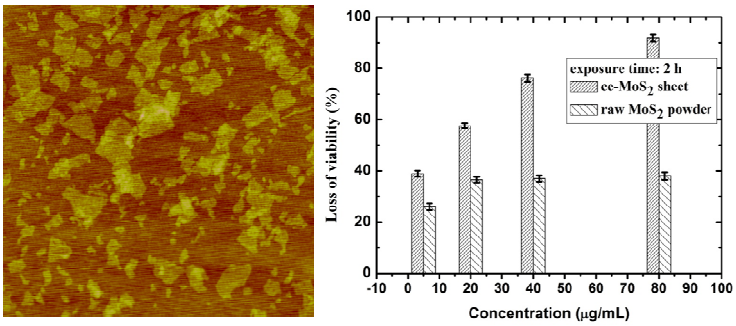

5